

Low-velocity shocks: signatures of turbulent dissipation in diffuse irradiated gas^{*}

P. Lesaffre¹, G. Pineau des Forêts^{2,1}, B. Godard³, P. Guillard⁴, F. Boulanger², and E. Falgarone¹

¹ ENS, LERMA, UMR 8112, CNRS, LRA/ENS, Observatoire de Paris, 24 rue Lhomond, 75005 Paris, France
e-mail: pierre.lesaffre@lra.ens.fr

² Institut d'Astrophysique Spatiale (IAS), UMR 8617, CNRS, Université Paris-Sud 11, Bâtiment 121, 91405 Orsay Cedex, France

³ Departamento de Astrofísica, Centro de Astrobiología, CSIC-INTA, Torrejón de Ardoz, Madrid, Spain

⁴ Spitzer Science Center (SSC), California Institute of Technology, MC 220-6, Pasadena, CA 91125, USA

Received 30 June 2012 / Accepted 5 November 2012

ABSTRACT

Context. Large-scale motions in galaxies (supernovae explosions, galaxy collisions, galactic shear etc.) generate turbulence, which allows a fraction of the available kinetic energy to cascade down to small scales before it is dissipated.

Aims. We establish and quantify the diagnostics of turbulent dissipation in mildly irradiated diffuse gas in the specific context of shock structures.

Methods. We incorporated the basic physics of photon-dominated regions into a state-of-the-art steady-state shock code. We examined the chemical and emission properties of mildly irradiated ($G_0 = 1$) magnetised shocks in diffuse media ($n_{\text{H}} = 10^2$ to 10^4 cm⁻³) at low- to moderate velocities (from 3 to 40 km s⁻¹).

Results. The formation of some molecules relies on endoergic reactions. Their abundances in J-type shocks are enhanced by several orders of magnitude for shock velocities as low as 7 km s⁻¹. Otherwise most chemical properties of J-type shocks vary over less than an order of magnitude between velocities from about 7 to about 30 km s⁻¹, where H₂ dissociation sets in. C-type shocks display a more gradual molecular enhancement with increasing shock velocity.

We quantified the energy flux budget (fluxes of kinetic, radiated and magnetic energies) with emphasis on the main cooling lines of the cold interstellar medium. Their sensitivity to shock velocity is such that it allows observations to constrain statistical distributions of shock velocities.

We fitted various probability distribution functions (PDFs) of shock velocities to spectroscopic observations of the galaxy-wide shock in Stephan's Quintet and of a Galactic line of sight which samples diffuse molecular gas in Chamaeleon. In both cases, low velocities bear the greatest statistical weight and the PDF is consistent with a bimodal distribution. In the very low velocity shocks (below 5 km s⁻¹), dissipation is due to ion-neutral friction and it powers H₂ low-energy transitions and atomic lines. In moderate velocity shocks (20 km s⁻¹ and above), the dissipation is due to viscous heating and accounts for most of the molecular emission. In our interpretation a significant fraction of the gas in the line of sight is shocked (from 4% to 66%). For example, C⁺ emission may trace shocks in UV irradiated gas where C⁺ is the dominant carbon species.

Conclusions. Low- and moderate velocity shocks are important in shaping the chemical composition and excitation state of the interstellar gas. This allows one to probe the statistical distribution of shock velocities in interstellar turbulence.

Key words. shock waves – astrochemistry – ISM: molecules – ISM: kinematics and dynamics – ISM: abundances

1. Introduction

Bulk motions in galaxies are generated for instance by supernovae explosions, galaxy collisions and galactic shear. These motions drive turbulence in the cold interstellar medium (ISM). A fraction of the available kinetic energy cascades down to smaller scales and lower velocities. This is spectacularly illustrated by the observations of the galaxy collision in Stephan's Quintet (SQ). The relative velocities of the galaxies (of about 1000 km s⁻¹) would be expected to dissipate in high-velocity shocks, thus creating a warm and hot plasma devoid of molecules. However, one observes that H₂ cooling is greater than the X-ray luminosity (Appleton et al. 2006; Cluver et al. 2010). This demonstrates that energy dissipation in the interstellar space involves an energy cascade and molecular gas cooling.

* Output data of models are available at the CDS via anonymous ftp to cdsarc.u-strasbg.fr (130.79.128.5) or via <http://cdsarc.u-strasbg.fr/viz-bin/qcat?J/A+A/550/A106> and at <http://cemag.ens.fr>

Moreover, the H₂ excitation diagram in SQ implies a distribution of temperatures much higher than the equilibrium temperature set by UV and cosmic ray heating. The same holds on much smaller scales in the case of the diffuse ISM in the solar neighbourhood (Gry et al. 2002; Ingalls et al. 2011). The range of gas temperatures can only be accounted for if the dissipation heats the gas through spatially localised events (Falgarone et al. 2005). This idea is also supported by observations of chemical species in the diffuse ISM such as CH⁺ and SH⁺, which cannot be reproduced by UV alone (Nehmé et al. 2008; Godard et al. 2012).

These dissipation processes have yet to be studied. Dissipative structures could for instance take the form of shocks, vortices, current sheets, or shear layers and most likely involve the magnetic field. This broad variety of processes, their different time scales and therefore different impacts onto the global gas energetics and chemistry call for simplified models to quantify observational diagnostics. Spectroscopy of molecular H₂ with Copernicus in the diffuse ISM motivated the first magnetohydrodynamics (MHD) shock models propagating in diffuse

gas. These first models were also the key to provide a first interpretation of CH^+ in the diffuse ISM (Mullan 1971; Draine et al. 1983; Flower et al. 1986; Gredel et al. 2002). Observations (Falgarone et al. 2005) by the instrument ISO-SWS of the pure rotational lines of H_2 in diffuse gas were also interpreted in the framework of mild turbulent dissipation (low-velocity MHD shocks and/or velocity shears in small-scale vortices). More recently, Godard et al. (2009) have modelled turbulent dissipation bursts in the diffuse ISM as vortices at very small scales and computed the chemical signatures they imprint on the gas.

In the present work, we use an updated version of the magnetised shock models of Flower & Pineau des Forêts (2003) to quantify composition and cooling lines for a range of shock velocities (from 3 to 40 km s^{-1}) including very low velocities that were not thoroughly considered before. We compute grids of these shocks for two strengths of the magnetic field and for three different densities. Our preshock conditions are representative of the cold diffuse ISM. Hence, we have incorporated the treatment of mild irradiation which includes UV heating, but also impacts the chemistry through photo-ionisation and photo-dissociation.

The shock velocity can be a crucial parameter even at very low velocity. Incidentally, the generation of molecules in the interstellar medium (ISM) is initiated by the formation of the H_2 molecule on dust grains surfaces. Then, the formation of more elaborate molecules relies on two main paths. One can either add a proton to H_2 to form H_3^+ and then transfer the extra proton to a single atom (C, O, S, and Si, with the notable exception of N). But H_3^+ is usually much less abundant than H_2 . Alternatively, one can directly exchange an atom with one proton of the H_2 molecule. But these reactions are subject to energy barriers with high characteristic temperatures (such as 2980 K in the case of the oxygen atom). Hence both paths are difficult and the observed molecular complexity of the ISM remains a puzzle. Nevertheless, temperatures required to open the second path are obtained in low-velocity shocks (7.5 km s^{-1} is enough to reach 3000 K). These shocks may therefore play an important role in shaping the molecular chemistry of the ISM.

The results of the present models may contribute to interpreting the observations of the full set of cooling lines of the cold neutral medium (CII, CI, OI, H_2 , CO, and H_2O) in galaxies observed with the *Spitzer* and *Herschel* space telescopes. To illustrate this, we built models from statistical distributions of shock velocities, which we compared to observed data in SQ and in a line of sight in the Chamaeleon (Gry et al. 2002). We use our best fit models to discuss the impact of kinetic energy dissipation on the physical state and chemistry of the molecular gas in these two sources. We also predict other diagnostic lines to be observed with *Herschel*.

We present the numerical method for our shock models in Sect. 2, with the properties of our grid of shocks in Sect. 3. In Sect. 4, we use our results to interpret the H_2 -excitation diagram observed in SQ and Chamaeleon. We summarise and discuss our results in Sect. 5.

2. Numerical method

The models we present in this paper are based on the plane-parallel steady-state shock code implemented in Flower & Pineau des Forêts (2003). We work from their version and include several more refinements mainly to deal with moderate irradiation.

2.1. Radiation

We started from the reactions network used in Flower & Pineau des Forêts (2003) and included the relevant photo-reactions. The photo-reactions have rates of the form

$$R = \alpha G_0 e^{-\beta A_v}, \quad (1)$$

where α and β are constants. We used an incident field equal to the standard interstellar radiation field (ISRF, Draine 1978), thus taking $G_0 = 1$. The extinction A_v is integrated along the model from the pre-shock where we use a value of $A_v = A_{v0} = 0.1$, which models extinction from the irradiation source by a “buffer” of matter. The value of A_{v0} is a parameter of the problem that selects how much mass is contained in this buffer. The local value for the extinction is then computed as

$$A_v = A_{v0} + \int_{x_0}^x dz \sigma_g n_H, \quad (2)$$

where $\sigma_g = 5.34 \times 10^{-22} \text{ cm}^3 \text{ pc}^{-1}$ is the effective extinction per H nuclei column density, n_H is the local density of H nuclei, x is the current position, and x_0 is the position at the entrance of the preshock (i.e. the point where we started our simulations). Our shocks are hence assumed to be irradiated “backward” compared to their direction of propagation. However, this matters only a little because the total extinction through these shocks is low (about $\Delta A_v = 0.01 (n_H/100 \text{ cm}^{-3})$, where n_H is the preshock density). This setup is indeed exactly similar to the one used by Bergin et al. (2004). However, these authors focused on the properties of a uniform-pressure photon-dominated region (PDR) following the shock, whereas we stop our computation immediately after the shock, and they considered pre-shock densities of $n_H = 1 \text{ cm}^{-3}$ much lower than we did.

The reaction rates for the photo-dissociation of H_2 and CO include an additional factor f_{shield} to account for the shielding and self-shielding. We used the tables of Lee et al. (1996) for CO and Draine & Bertoldi (1996) for H_2 with a Doppler parameter

$$b_D = \sqrt{u_{\text{th}}^2 + u_{\text{turb}}^2}, \quad (3)$$

where u_{th} is the thermal velocity of H_2 molecules and $u_{\text{turb}} = 1 \text{ km s}^{-1}$ accounts for microturbulence. However, we neglect the effect of velocity gradients on the self-shielding. For instance:

$$R_{\text{H}_2+h\nu} = (2.54 \times 10^{-11} \text{ s}^{-1}) f_{\text{shield}} e^{-6.3 A_v}, \quad (4)$$

where

$$f_{\text{shield}} = \frac{0.965}{(1 + x/b_D)^2} + \frac{0.035 e^{-8.5 \times 10^{-4} \sqrt{1+x}}}{\sqrt{1+x}}, \quad (5)$$

with $x = N(\text{H}_2)/(5 \times 10^{14} \text{ cm}^{-2})$. Here, the quantity $N(\text{H}_2)$ is the column density of H_2 molecules, computed in the same way as for the extinction:

$$N(\text{H}_2) = N_0(\text{H}_2) + \int_{x_0}^x dz n(\text{H}_2) \quad (6)$$

where $n(\text{H}_2)$ is the local density of H_2 molecules and $N_0(\text{H}_2)$ is the quantity of H_2 molecules in the buffer that shields the medium from the external radiation field. We match $N_0(\text{H}_2) \simeq 10^{20} \text{ cm}^{-2}$ to $A_{v0} = 0.1$ by assuming this buffer is mainly molecular. Similarly, we define $N_0(\text{CO})$ for the CO self-shielding but

Table 1. Values for the main physical parameters in our models.

Parameter	Value	Comment
n_{H}	$10^2, 10^3$ or 10^4 cm^{-3}	H nuclei pre-shock density
u	3 to 40 km s^{-1}	Shock velocity
$b = B/n_{\text{H}}^{1/2}$	0.1 or 1	Dimensionless magnetic field
$A_{\text{r}0}$	0.1	Buffer extinction
$N_0(\text{H}_2)$	10^{20} cm^{-2}	Buffer H_2 column density
$N_0(\text{CO})$	0	Buffer CO column density
G_0	1	External radiation field
ζ	$3 \times 10^{-17} \text{ s}^{-1}$	Nominal cosmic rays flux
OPR	3	Preshock H_2 ortho/para ratio

use $N_0(\text{CO}) = 0$ because $A_{\text{r}0} = 0.1$ is usually well below the extinction at which CO is self-shielded in standard models of PDR.

With this irradiation model, we integrated the chemical and thermal evolution of a fluid parcel with fixed density moving away from the radiation source at a constant velocity v_{PDR} where the subscript PDR refers to the PDR. The resulting spatial profile (the trace of the thermal and chemical composition history of this fluid parcel along its path) corresponds to a steady PDR front moving towards the irradiation source at speed v_{PDR} . For very low velocities we recover a steady PDR front that compares quite satisfactorily to the Meudon PDR code (Le Petit et al. 2006) for $G_0 = 1$. In the frame of this comparison we switched off grains and polycyclic aromatic hydrocarbons (PAHs) reactions to remain closer to the Meudon PDR code setup. The PDR structure is insensitive to the choice of Lee et al. (1996) or Draine & Bertoldi (1996) for H_2 photo-dissociation. This is because the rates differ only in regions where the absolute value of the rates are low, hence unimportant. For the same reason, we expect that our results only weakly depend on the exact value of the above mentioned Doppler parameter b_{D} . Black & van Dishoeck (1987) also showed that this parameter is not crucial in PDRs.

Compared to Flower & Pineau des Forêts (2003), we refreshed the collision rates of OI by H atoms with the rates computed by Abrahamsson et al. (2007). These rates enter the computation of the atomic cooling due to O atoms. Atomic and molecular cooling are otherwise identical to those employed in Flower & Pineau des Forêts (2003). For instance, we used the molecular cooling rates tabulated in Neufeld & Kaufman (1993) for the cooling by CO and H_2O .

2.2. H_2 -excitation

We followed the time-dependent excitation of H_2 along the shock structure as detailed in Flower & Pineau des Forêts (2003). Here, we include the treatment of the H_2 population for the 149 lowest energy levels. We checked that this allows us to compute the H_2 cooling accurately for shock velocities up to at least 40 km s^{-1} for the range of densities we consider in this work (see also Flower & Pineau des Forêts 2003).

We also used the knowledge of the population of the eight lowest H_2 rotational levels to compute the rate of the reaction $\text{C}^+ + \text{H}_2$ more accurately. To compute the rate state by state, we used the information in Gerlich et al. (1987) (as in Agúndez et al. 2010, line 2 of Table 1) for H_2 levels with $J = 0 \dots 7$ and $v = 0$ and the information in Hierl et al. (1997) (as in Agúndez et al. (2010), line 3 of Table 1) for the other levels.

2.3. Grains

As in Flower & Pineau des Forêts (2003), we treated adsorption, collisional sputtering, and collisional desorption of molecules from and onto grains. However, unlike these authors, we assumed pre-shock conditions without ice mantles. We accounted for the charge of grains by including all charge exchanges involving grains and electron detachment by cosmic-ray-induced secondary photons. The heating through the photo-electric effect was included, but we discarded the detachment of electrons that is caused by the radiation field in the chemical network.

3. Grid of models

3.1. Numerical protocol

For each value of our parameters described in the next section, we integrated the steady-state equations of multi-fluid MHD shocks (Flower et al. 1985; Heck et al. 1990) from entrance conditions at thermal and chemical equilibrium (see details of the pre-shock chemical conditions below). As stated above, we accounted for the changes in the properties of the irradiation field caused by the increasing absorption as we penetrated deeper into the shock structure. The computation was stopped when the temperature decreased to 20% above the temperature of the pre-shock.

3.2. Choice of parameters

We tuned most of our parameters to the typical conditions encountered in the dilute interstellar gas in our galaxy. We list the main physical parameters of our model in Table 1.

We indirectly specified the strength of the magnetic field transverse to the shock speed by using the nondimensional parameter $b = (B/1 \mu\text{G})/\sqrt{n_{\text{H}}/\text{cm}^{-3}}$, which Crutcher et al. (2010) observed to take values from $b = 0.1$ to $b = 1$ for our range of densities. We refer to these values below by highly magnetised shocks for $b = 1$ and weakly magnetised shocks for $b = 0.1$.

For both of these assumptions on the magnetic field, we built three grids of models, one for each pre-shock density between $n_{\text{H}} = 10^2 \text{ cm}^{-3}$, $n_{\text{H}} = 10^3 \text{ cm}^{-3}$, and $n_{\text{H}} = 10^4 \text{ cm}^{-3}$. In the following, we will use the term *low* velocity for shocks below 20 km s^{-1} , *moderate* velocity for shocks exceeding 20 km s^{-1} , and *high* velocity for shocks at and higher than 40 km s^{-1} . Each grid spans a range of velocities from 3 to 40 km s^{-1} with steps of 0.5 km s^{-1} for an integration time of about six hours per grid on a typical workstation. We chose our lowest velocity of 3 km s^{-1} above the Alfvén speed in the neutral gas for $b = 1$

$$v_{\text{A}} = \frac{B}{\sqrt{4\pi\rho}} = \frac{b}{\sqrt{4\pi(\mu_{\text{H}}/\text{a.m.u.})}} = 1.85b \text{ km s}^{-1} \quad (7)$$

where the mean mass per H nucleus is $\mu_{\text{H}} = \rho/n_{\text{H}} = 1.4 \text{ a.m.u.}$. We chose the upper bound of 40 km s^{-1} because of the limitations of our shock models¹.

At each fixed pre-shock density, we first evolved the gas chemically and thermally during 10^7 years, which brings the gas close to thermal and chemical equilibrium. We started with the same elemental abundances as in Godard et al. (2009), which are summarised in Table 2. The gas phase abundance in the pre-shock is set to a tenth of the Si locked in the grains cores, consistent with observations (Jenkins 2009). We also included PAHs

¹ Indeed, the code does not treat doubly ionised species and radiative emission from the post-shock itself, which might affect pre-shock conditions at high densities (see Flower & Pineau des Forêts 2010).

Table 2. Elemental composition of the pre-shock gas (as in Godard et al. 2009).

Element X	Fractional value $n(X)/n_{\text{H}}$			
	Total	Gas	Grain cores	PAHs
H	1	1		1.80(-5)
He	0.1	0.1		
C	3.56(-4)	1.38(-4)	1.63(-4)	5.40(-5)
O	4.42(-4)	3.02(-4)	1.40(-4)	
N	7.94(-5)	7.94(-5)		
Mg	3.70(-5)		3.70(-5)	
Si	3.70(-5)	3.37(-6)	3.37(-5)	
S	1.86(-5)	1.86(-5)		
Fe	3.23(-5)	1.50(-8)	3.23(-5)	

Notes. Initial conditions assume no ice mantles (bare cores). The gas to dust mass ratio is $\rho_{\text{gas}}/\rho_{\text{dust}} \approx 180$. The numbers in parentheses denote powers of ten.

with a fraction $n(\text{PAH})/n_{\text{H}} = 10^{-6}$ of the representative species $\text{C}_{54}\text{H}_{18}$. Without irradiation ($G_0 = 0$), PAHs influence the ionisation degree of the gas and the charge-ion coupling. However, with mild irradiation (at $G_0 = 1$) the C^+ ions dominate the charge fluid and the role of PAHs is negligible. With our current irradiation parameters (G_0 , extinction and H_2 buffer), the atomic hydrogen fraction is $n(\text{H})/n_{\text{H}} = 7.9(-2)$, $1.3(-2)$ and $2.0(-3)$ in the preshock gas with respective densities $n_{\text{H}} = 10^2 \text{ cm}^{-3}$, 10^3 cm^{-3} and 10^4 cm^{-3} . We then used the resulting state as our pre-shock conditions to run the shock model for each velocity in turn.

3.3. C- and J-type shocks

Steady-state magnetised shocks in the interstellar medium are of two kinds: J-type shocks in which the kinetic energy is dissipated viscously in a very sharp velocity *jump* (hence “J”) followed by a thermal and chemical relaxation layer, and C-type shocks in which kinetic energy is *continuously* (hence “C”) degraded into heat and photons via ion-neutral friction and cooling. Mullan (1971) was first to discover that strong magnetic fields can transfer kinetic energy to thermal energy in a continuous manner and coined the term C shock. Draine (1980), Draine et al. (1983), and Roberge & Draine (1990) then described the multifluid nature of these shocks. C shocks occur as long as the shock velocity remains below the propagation speed of the magnetic precursor. This critical velocity above which a C shock cannot exist is the magnetosonic velocity

$$v_{\text{m}} = \sqrt{c_{\text{s}}^2 + v_{\text{Ac}}^2}, \quad (8)$$

where $v_{\text{Ac}} = B/\sqrt{4\pi\rho_{\text{c}}}$ is the Alfvén speed in the *charged* fluid and c_{s} is the speed of sound. The Alfvén speed in the charges depends both on the magnetic field and on the inertia in the charged fluid. Thanks to the irradiation field, the gas is well ionised and provides ample free electrons to stick onto the grains. As a result, most grains are charged negatively in our models and hence they dominate the inertia in the charged fluid. Moreover, Guillet et al. (2007) showed that even the neutral grains spend an extensive fraction of their time attached to the magnetic field and should also be included in the charged fluid inertia. We hence included all PAH and grains in the computation of the magnetosonic speed. As a result, the Alfvén speed in the charged fluid v_{Ac} is higher than v_{A} by a factor $v_{\text{Ac}} \sim \sqrt{\rho/\rho_{\text{d}}} v_{\text{A}}$, where $\rho/\rho_{\text{d}} \sim 180$ is the gas-to-dust mass ratio. The actual number in our simulations is $v_{\text{m}} = 21.2 \text{ km s}^{-1}$, 21.7 km s^{-1} , and 22.9 km s^{-1} for

$n_{\text{H}} = 10^2 \text{ cm}^{-3}$, 10^3 cm^{-3} , and 10^4 cm^{-3} for $b = 1$ and about ten times lower values for $b = 0.1$.

Shocks with speeds greater than v_{m} will always be J shocks. For instance, all shocks in our $b = 0.1$ grid are J shocks. However, time-dependent shocks with velocities lower than v_{m} could be C shocks, J shocks, or even a combination of the two (see Chièze et al. 1998; Lesaffre et al. 2004a,b). Indeed, (i) the transverse magnetic field could be lower for various orientations of the field (see Wardle 1998 for oblique C shocks); (ii) or the C shock could be at an earlier development of its structure where it still has a J shock component (Chièze et al. 1998; Lesaffre et al. 2004a); (iii) or the final fate of the shock could be a steady-state CJ shock, depending on the history of the shock (Lesaffre et al. 2004a,b). As a result, we built our grids of models with C shocks for shock velocities up to v_{m} and used J shocks for higher shock velocities. In the following, we explore the properties of the resulting shocks.

3.4. Weakly magnetised shocks ($b = 0.1$)

For high compression ratios (i.e. Mach numbers much greater than 1), the maximum temperature in a J shock (obtained just behind the leading adiabatic shock front) is

$$T_{\text{max}} = \frac{2(\gamma - 1)}{(\gamma + 1)^2} \frac{\mu}{k_{\text{B}}} u^2, \quad (9)$$

where μ is the mean molecular weight of the gas, k_{B} is the Boltzmann constant, and u is the shock velocity in the shock frame. The shock velocity is very close to the velocity difference between upstream and downstream gas for high Alfvénic Mach number. In particular, this relation shows that the peak temperature in a shock is proportional to the square of the shock velocity.

For such dilute molecular gas, only the lowest energy levels of H_2 are populated and the appropriate value for γ is $\gamma = 5/3$. With $\mu = 2.33 \text{ a.m.u.}$ (which corresponds to the above $\mu_{\text{H}} = 1.4$ in our almost fully molecular conditions) relation (9) becomes

$$T_{\text{max}} = 53 \text{ K} (u/1 \text{ km s}^{-1})^2. \quad (10)$$

Figure 1a displays this theoretical value and the actual maximum temperature reached in our models for each velocity tested in our grid at $n_{\text{H}} = 10^2 \text{ cm}^{-3}$. Both values remain close to one another. At high temperature (high velocity), the maximum temperature is closer to the value obtained in Eq. (9) with $\gamma = 7/5$. This stems from the excitation of rotational levels of the H_2 molecules in the adiabatic front. We used a viscous length $\lambda = 1/\sigma n_{\text{H}}$ with a viscous cross-section $\sigma = 3 \times 10^{-15} \text{ cm}^2$ based on H_2 - H_2 collision data computed by Monchick & Schaefer (1980) for a velocity dispersion of 1 km s^{-1} . We checked that the viscous front between the peak temperature and the pre-shock is always adiabatic. Its width of 10^{13} cm , visible in Fig. 1b, corresponds to the viscous length for $n_{\text{H}} = 10^2 \text{ cm}^{-3}$. This figure surprisingly shows that higher velocity shocks return to pre-shock temperature on a smaller distance than low-velocity shocks. However, the range of scales spans only one order of magnitude from $2 \times 10^{15} \text{ cm}$ to $2 \times 10^{14} \text{ cm}$ with all shocks with velocities higher than 20 km s^{-1} around the scale of $2 \times 10^{14} \text{ cm}$. The range of flowing time through these shock structures also spans about one order of magnitude, from 400 yr to 2000 yr. For higher densities, the picture is much the same, and in particular time scales vary little within one category (J-type or C-type) of shocks. However, shocks that strongly dissociate H_2 (such as dense shocks at moderate velocity) have a wide H_2 reformation plateau where H_2

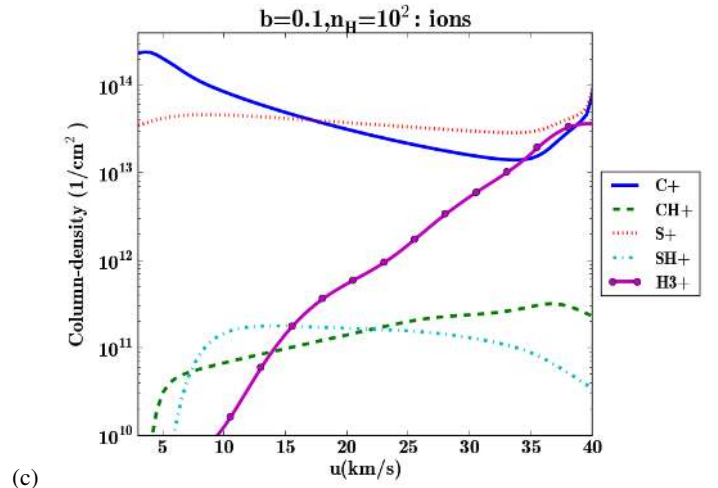
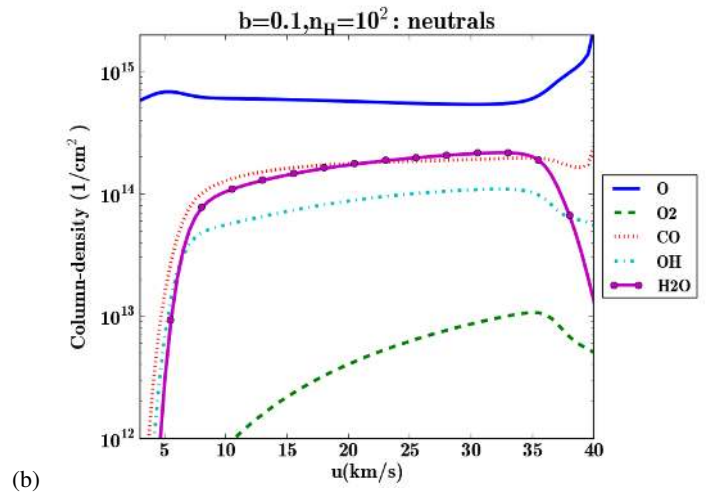
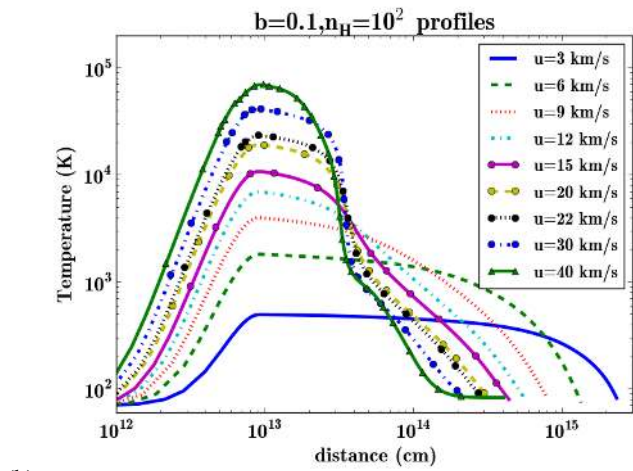
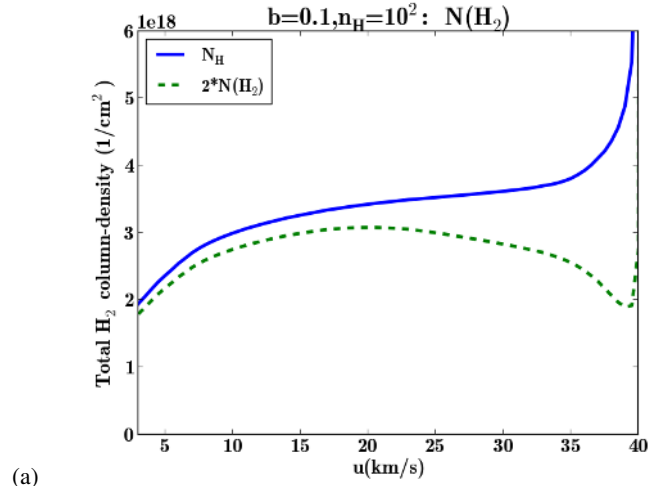
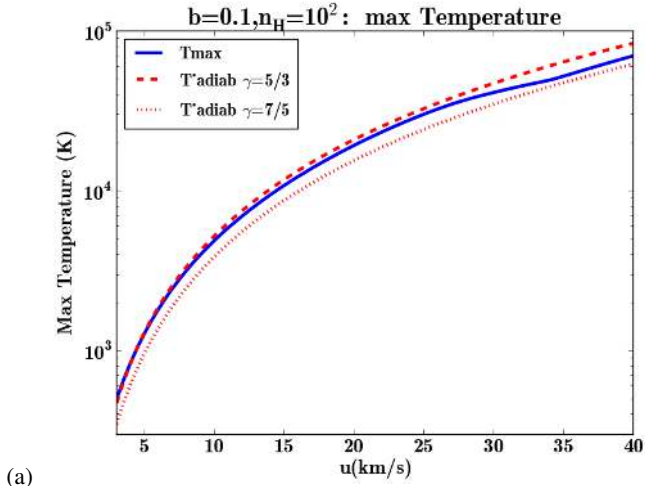


Fig. 1. a) Maximum temperature in the *weakly magnetised* shocks. b) Temperature profiles for some representative *weakly magnetised* shocks, the fluid flows from left to right with the pre-shock on the left and the post-shock on the right. Only J shocks are present for this low value of the magnetic field. $n_{\text{H}} = 10^2 \text{ cm}^{-3}$.

reformation provides the necessary heat to keep the gas warm (Flower et al. 2003).

Figure 2a shows the total column density of H nuclei (N_{H}) across each shock in the grid. Also displayed is the total H_2 column density. The total N_{H} column density is surprisingly constant around $N_{\text{H}} = 3\text{--}4 \times 10^{18} \text{ cm}^{-2}$ over the range of velocities in our grid except at the two ends. The increase of the compression factor at higher shock speed is compensated for by the shorter cooling length. This result is in contrast to the results obtained by Hollenbach & McKee (1989) in the velocity range 30 to 150 km s^{-1} , where the cooling column density behind the shocks is seen to vary greatly. Shocks with velocities below about 7 km s^{-1} have a lower than average total column density, and shocks with velocities above 35 km s^{-1} dissociate H_2 , which decreases the amount of cooling and increases the total column density.

Figures 2b and c show the total column densities across the shock for various neutrals and ions. We recall that the end of each shock is defined as the moment when the temperature decreases to 20% above the pre-shock temperature. Since the overall column density is a slowly varying function of the shock velocity (Fig. 2a), these plots also give a good estimate on how

Fig. 2. For each shock velocity in our *weakly magnetised* shocks ($b = 0.1$), we plot a) the total H nuclei and H_2 molecules column densities b) some neutrals of interest and c) some ions of interest; $n_{\text{H}} = 10^2 \text{ cm}^{-3}$.

the average relative abundance of each of these species varies with respect to the shock velocity. One striking feature of these figures is the sharp rise of some molecular abundances at low velocity. We traced these apparent velocity thresholds to temperature barriers or endothermicities of key reactions that initiate the production of molecules. Equation (10) allows us to relate

Table 3. List of bottleneck reactions for molecule formation with their temperature barrier or endothermicity and the corresponding velocity of the J-type shock that is able to provide this temperature computed using Eq. (10).

Reaction	Temperature barrier	Velocity
$O+H_2 \rightarrow OH+H$	2980 K	7.5 km s ⁻¹
$C^++H_2 \rightarrow CH^++H$	4640 K	9.4 km s ⁻¹
$S+H_2 \rightarrow SH+H$	9620 K	13.5 km s ⁻¹
$S^++H_2 \rightarrow SH^++H$	9860 K	13.6 km s ⁻¹
$C+H_2 \rightarrow CH+H$	14 100 K	16.3 km s ⁻¹
$Si^++H_2 \rightarrow SiH^++H$	14 310 K	16.4 km s ⁻¹
$N+H_2 \rightarrow NH+H$	14 600 K	16.6 km s ⁻¹
H ₂ dissociation energy	52 000 K	31.3 km s ⁻¹

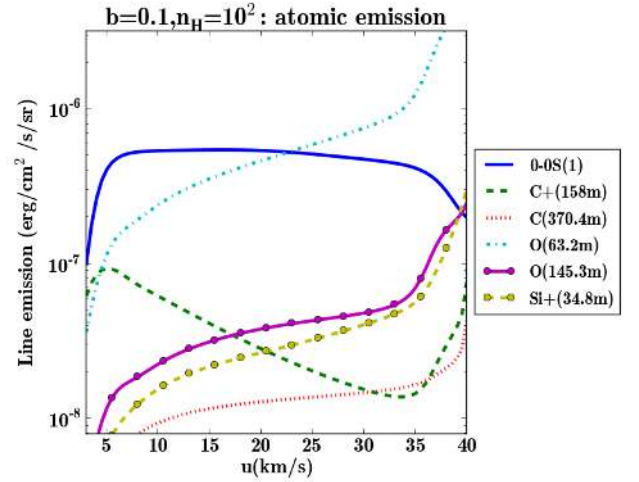
Notes. N⁺ + H₂ has little or no barrier: 168 K.

these critical temperatures to the key velocities in J shocks. We list in Table 3 the main bottleneck reactions that involve H₂ and a single atom or monoatomic ion along with their characteristic temperatures and J shock velocities. At high velocities, the decrease in molecular content (around 35 km s⁻¹) corresponds to the absence of H₂ molecules due to dissociation in the shock front.

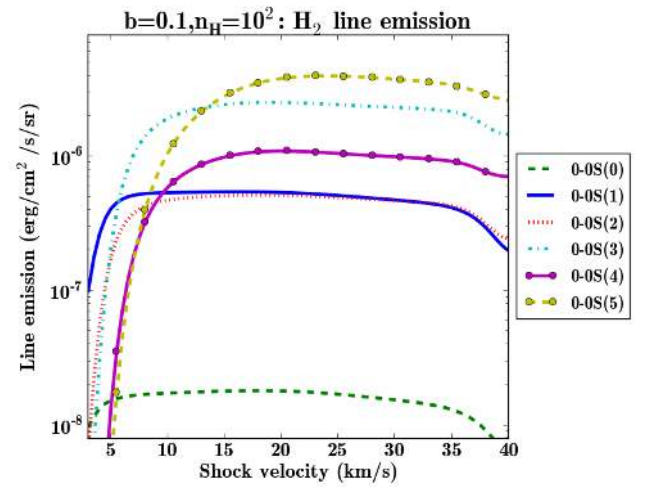
Figure 2c illustrates the variation of a few ions of interest. The abundance of C⁺ is controlled mainly by photo-ionisation of C and charge exchange with PAHs and H₂. As the velocity increases, the post-shock density increases with enhanced charge exchange, thus decreasing the C⁺ abundance. For very high velocities (above 35 km s⁻¹) H₂ starts to be dissociated and C⁺ increases again. In a molecular medium, the abundance of H₃⁺ is controlled by the balance between cosmic ray ionisation of H₂ (followed by a hydrogen exchange with H₂) and recombination of H₃⁺. The charge balance links the ionisation degree to the abundance of C⁺, thus the abundance of H₃⁺ is inversely proportional to C⁺ with an extra dependence on the square root of the temperature due to the temperature sensitivity of the recombination rate.

In Fig. 3 we display the variation of the total emission of various lines of interest depending on the shock velocities. This can be of interest for observers who aim to characterise the velocities of observed shocks. Figure 3a shows some of the most observed atomic lines with the H₂ 0-0 S(1) line for comparison. The C⁺ ion emission decrease at moderate velocities is an abundance effect. Atomic O cooling is enhanced at moderate velocities because these shocks dissociate H₂: this slows down the cooling and yields a temperature plateau where O is the dominant cooling agent. The stronger the shock, the longer it takes for H₂ to reform, then the plateau widens and the O emission increases.

Figure 3b shows how the lowest energy lines of H₂ change with the velocity of the shock. The relative strengths of these lines vary greatly between $u = 3$ km s⁻¹ and $u = 10$ km s⁻¹. For example, the ratio S(1)/S(3) decreases from more than a hundred at 3 km s⁻¹ to about a fifth at 10 km s⁻¹. Indeed, the shock peak temperature in this range of velocities spans the energies of the upper levels of these transitions ($J = 7$ corresponds to 3474 K, for instance, and see Fig. 1a for how the maximum temperature in the shock varies with shock velocity): the excitation diagram in the low levels of H₂ is greatly affected in this range of temperatures. By contrast, the aspect of the excitation diagram does not change above 10 km s⁻¹: the emissivities of these lines are unable to distinguish the shock velocity u for $u > 10$ km s⁻¹.



(a)



(b)

Fig. 3. a) Atomic and b) pure rotational H₂ line emission for weakly magnetised shocks. $n_H = 10^2$ cm⁻³.

Indeed, above 10 km s⁻¹ the temperature experienced in these shocks is much greater than the $J = 7$ energy. Observers should use lines with upper levels with higher J values (such as rovibrational lines) to probe the velocities of these shocks, or they should use diagnostics based on atomic lines.

In Fig. 4 we examine that fraction of the kinetic energy flux input

$$I_{\text{kinetic}} = \frac{1}{2} \rho u^3 \quad (11)$$

into the shock that is radiated away by each coolant. Individual coolings are integrated through the whole shock structure as follows:

$$I_{\text{cool}} = \int_{x_0}^{x_1} \Lambda dz, \quad (12)$$

where Λ is the local rate of cooling and x_1 is the end point of the shock (i.e. where the temperature decreases to 20% above the pre-shock temperature). We also display the magnetic energy flux across the shock,

$$I_{\text{Bflux}} = \frac{B_c^2}{4\pi} u_i, \quad (13)$$

where u_i is the ion velocity and B_c is the magnetic field at the end of the shock. H₂ cooling dominates almost everywhere except (i)

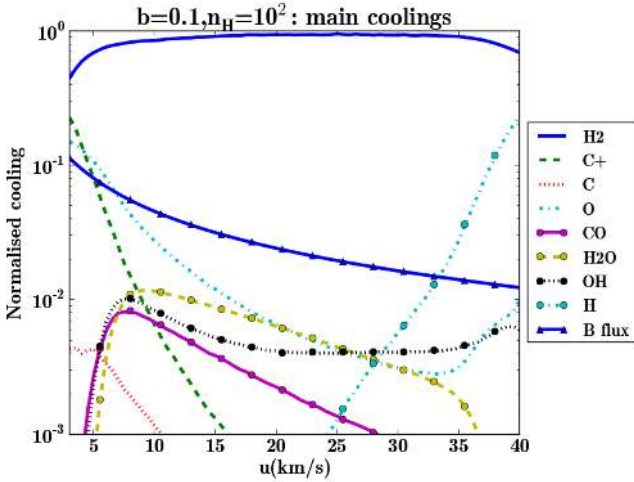


Fig. 4. Cooling integrated along the shock length, normalised by kinetic power $\frac{1}{2}\rho u^3$ in *weakly magnetised* shocks, for $n_{\text{H}} = 10^2 \text{ cm}^{-3}$. The solid line with triangles shows the fraction of the power that is transferred into a flux of magnetic energy. In this figure, H_2 cooling incorporates the cooling from 200 lines between the 149 H_2 levels included in the simulation, whereas Fig. 3 considers only six individual lines amongst the lowest levels of H_2 .

at very low velocity, where atomic O or C^+ cooling takes over depending on the density; and (ii) above the velocity for H_2 dissociation (which is lower for higher densities), where atomic O and H (Lyman- α) cooling take over. At density $n_{\text{H}} = 10^4 \text{ cm}^{-3}$, and below 20 km s^{-1} , note that H_2O cooling becomes important.

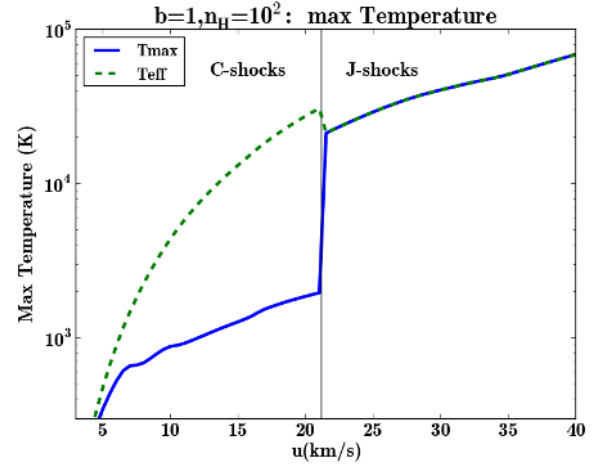
3.5. Strongly magnetised shocks ($b = 1$)

In a C shock, the kinetic energy is continuously transformed into thermal energy via ion-neutral friction. As a result, the heating is spread out on a much more extended region than for J shocks and the peak temperature is hence much lower as seen in Fig. 5a. However, reactions between neutral and ion species benefit from the ion-neutral drift, and the effective temperature that is used to compute the reaction rate is higher (see Pineau des Forêts et al. 1986). For instance, the effective temperature for reactions involving C^+ and H_2 is

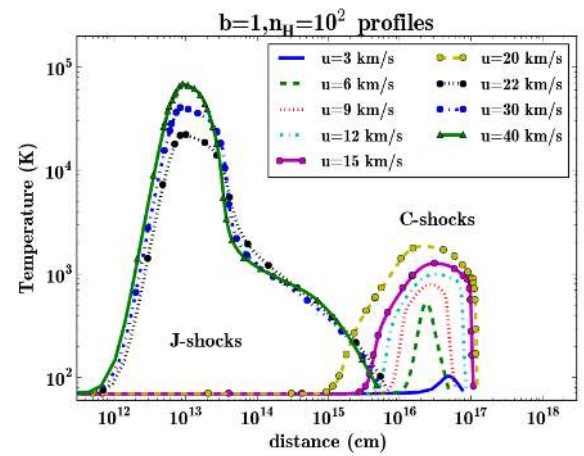
$$T_{\text{eff}}(\text{C}^+, \text{H}_2) \simeq \frac{2T_{\text{n}} + 12T_{\text{i}}}{2 + 12} + \frac{2 \times 12}{2 + 12} \frac{m_{\text{p}}}{3k_{\text{B}}} (u_{\text{n}} - u_{\text{i}})^2 \quad (14)$$

where $(u_{\text{n}} - u_{\text{i}})$ is the local drift velocity between the ions and the neutrals, m_{p} is the proton mass and T_{n} and T_{i} are respectively the temperatures of the neutral and ionised gas. Figure 5a shows the maximum effective temperature of the reaction $\text{C}^+ + \text{H}_2$, which incidentally is very close to the highest temperature that would be obtained in the corresponding J shock.

Compared to the temperature profile of a J shock, the temperature profile of a C shock is broad, with a lower temperature: see Fig. 5b. However, within each type of shock, the total size of the shock structure varies over less than an order of magnitude for the range of velocities we tested, as is apparent in Fig. 5b. This is even more striking for the flowing time scale across the shock structures which, for $n_{\text{H}} = 10^2 \text{ cm}^{-3}$, varies only from 8000 to 6000 years for the C shocks and from 1500 to 1000 years for the J shocks. As mentioned above, this holds for higher densities as well.



(a)



(b)

Fig. 5. a) Highest temperature in the *highly magnetised* shocks. b) Temperature profiles for some representative *highly magnetised* shocks; the fluid flows from left to right with the pre-shock on the left and the post-shock on the right; $n_{\text{H}} = 10^2 \text{ cm}^{-3}$.

Slightly above 20 km s^{-1} , all shocks in our grids of models are J shocks, but the strength of the magnetic field varies from $b = 0.1$ in the previous subsection to $b = 1$ in this subsection. The higher magnetic field limits the compression in the shock and the collisional processes take longer to occur. In particular, the cooling length for the J shocks above 20 km s^{-1} is between $4 \times 10^{15} \text{ cm}$ and $7 \times 10^{15} \text{ cm}$: much wider than for the corresponding weakly magnetised J shocks. The lower density but larger size of the shock impacts on the chemical composition and structure in subtle ways. A careful comparison of the right hand sides of Figs. 2 and 6 shows that the column density of H nuclei is higher in magnetised shocks and moderate variations in the chemical composition are noticeable.

Figure 6 shows the molecule production over the range of models in our grid at $n_{\text{H}} = 10^2 \text{ cm}^{-3}$. The transition from C shocks (velocity lower than 21 km s^{-1}) to J shocks (higher shock speed) is clear. The column densities of most species have a drop at 21 km s^{-1} that expresses a boosted molecular production in C shocks. Three effects are at play that favour molecule production in C shocks.

First, the ion-neutral drift helps to overcome reaction barriers of ion-neutral reactions (which impact C-bearing species, for example, whose bottleneck reaction is $\text{C}^+ + \text{H}_2$). Second, the resulting frictional heating keeps the temperature warm throughout the shock. By comparison, a J shock is very hot at the peak

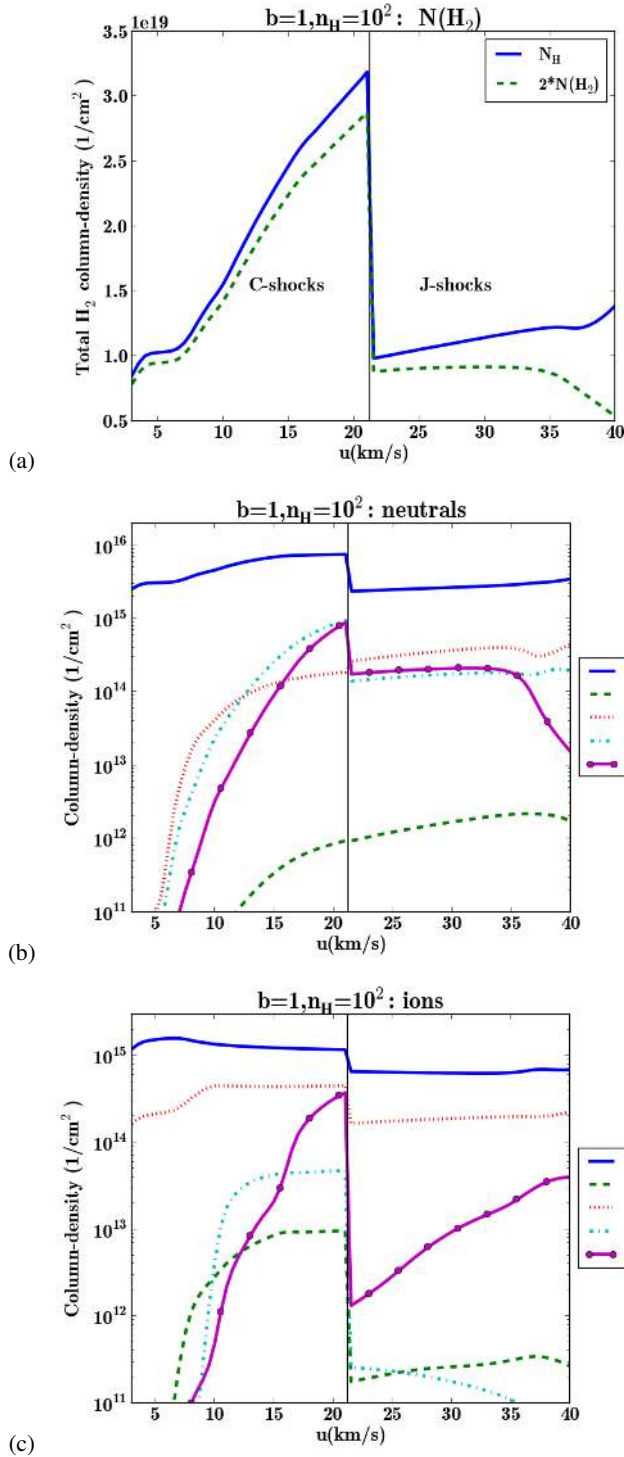


Fig. 6. Same as Fig. 2 for highly magnetised shocks ($b = 1$). $n_H = 10^2 \text{ cm}^{-3}$.

temperature immediately behind the viscous front, but quickly cools down in the trailing relaxation layer. Third, the steady frictional heating slows down cooling and compression in the relaxation layer, and the net result is an increased total N_H column density in C shocks compared to J shocks (see the drop at 21 km s^{-1} in Fig. 6a). This is the main factor that impacts those molecular species whose production relies mainly on neutral-neutral reactions (such as O-bearing species). In particular, these species show a more gradual rise at low velocities, because of the slower rise of the maximum neutral temperature in C shocks.

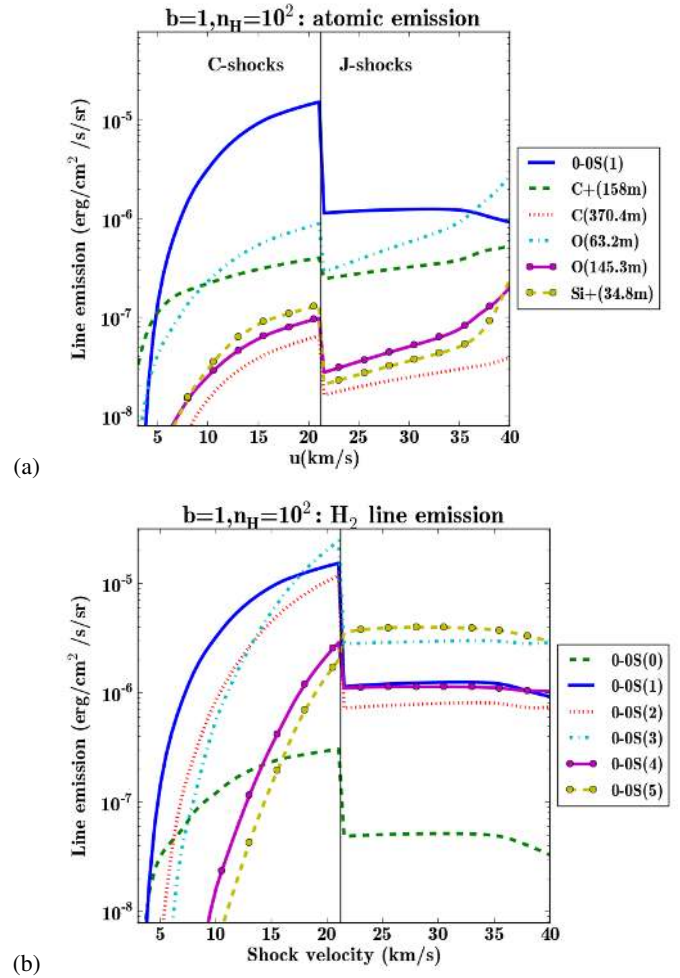


Fig. 7. a) Atomic and b) rotational H_2 lines emission for highly magnetised shocks. $n_H = 10^2 \text{ cm}^{-3}$.

We display the total integrated emission in various lines of interest in Figs. 7a and b: as for Fig. 3, these give clues on which observations constrain what shock velocity. In particular, the emissivities of H_2 lines with low-J upper levels now vary from 3 to 20 km s^{-1} , but are independent of velocity above 20 km s^{-1} . The neutral temperature in C shocks rises more slowly than J shocks, as shown by the comparison between Figs. 1 and 5, but the maximum temperature in C shocks is more representative of the temperature in the whole mass of the shock and the column density in C shocks is higher. As a result, the left hand sides (between 3 and 20 km s^{-1}) of Figs. 7a and b look like blow ups of Figs. 3a and b shifted to greater emissivities. However, C^+ stands out even more for C shocks because its excitation benefits from the ion-neutral drift. The right-hand sides of Figs. 7a and b are similar to the corresponding weakly magnetised J shocks seen in Figs. 3a and b: the emissivities are only weakly affected by the density change caused by the magnetic field except for C^+ .

In Fig. 8 we examine, averaged over the whole shock structure as in Fig. 4, the fraction of the kinetic energy flux input into the shock that is radiated away by each coolant in the low-density case ($n_H = 10^2 \text{ cm}^{-3}$). At very low velocity, C^+ is the most efficient coolant (rather than O for weakly magnetised shocks), but H_2 takes over for shock velocities shortly above 5 km s^{-1} . Molecules such as CO, H_2O , or OH carry less than a percent of this energy flux. The kinetic energy flux is mainly

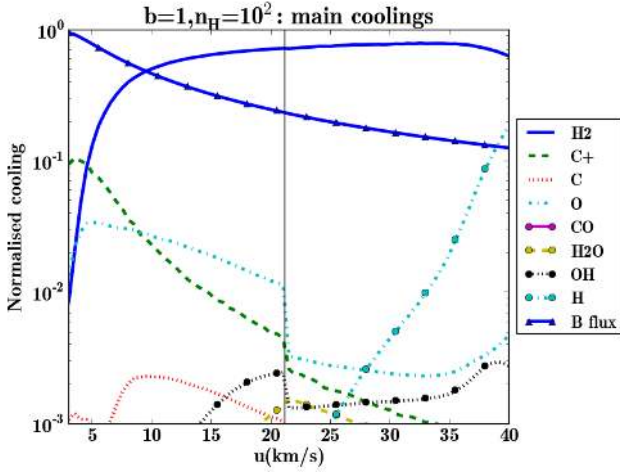


Fig. 8. Cooling normalised by kinetic power in *highly magnetised* shocks for a pre-shock density $n_{\text{H}} = 10^2 \text{ cm}^{-3}$. The solid line with triangles shows the fraction of the power that is transferred into a flux of magnetic energy.

transferred into a magnetic energy flux (via field compression) for velocities below 10 km s^{-1} and is mainly radiated away above that velocity. At higher densities, the low-velocity coolant becomes O. It is also interesting to note that at $n_{\text{H}} = 10^4 \text{ cm}^{-3}$ H_2O becomes an important cooling agent for low velocities. Flower & Pineau des Forêts (2010) also quoted the fraction of energy radiated away in various cooling processes in their shock models. However, in the present work the irradiation field photo-dissociates CO and ionises C so that C^+ cooling is more prominent and CO cooling is less important than in their work, but the results are otherwise similar. In particular, Flower & Pineau des Forêts (2010) also found that the magnetic energy flux stores 50% of the injected power at $u = 10 \text{ km s}^{-1}$.

4. Probability distribution functions of shocks

4.1. Method of fit

Numerical simulations of driven supersonic turbulence show that the medium experiences a whole range of shock speeds: Smith et al. (2000) showed that the probability distribution function (PDF) of the velocity jumps follows a decreasing power law with an exponential cut-off at a Mach number of a few. Pety & Falgarone (2000) carefully separated vortical from compressional contributions in the velocity field of a compressible simulation of decaying supersonic turbulence: they uncovered an exponential distribution for the convergence time scales $-1/\text{div}(v)$ where v is the fluid velocity. Subsonic wind tunnel experiments displayed an exponential distribution of velocity increments (Mouri et al. 2008).

These results hint at a variety of possible PDF shapes for the statistics of shocks, all favourably weighted towards low-velocity shocks. Guillard et al. (2009) have modelled *Spitzer* H_2 observations of SQ with only two discrete values of the shock velocities. Here, we aim at fitting a statistical distribution of shocks to a collection of observed quantities. Guided by the above remarks on turbulence, we fitted various shapes of shock PDFs: decaying exponentials, power-laws, Gaussians, and a piece-wise exponential fit.

We considered among $j = 1 \dots M$ observable quantities an observable $X_j(u)$ associated to a steady shock of velocity u (expressed in km s^{-1}). We denote with $f(u, \{p_i\}_{i=1 \dots N})$

Table 4. Template PDFs adjusted to the observed data (normalisation constants are discarded as irrelevant, see text).

PDF	Formula	N
Power-Law	u^{-p_1}	1
Exponential	$\exp(-p_1 u)$	1
Piece-wise exponential	at $u = 3, 10, 20, 40$ $f(u) = 1, p_1, p_2, p_3$	3
one-Gaussian	$e^{-(u-p_1)^2}$	1
two-Gaussian	$e^{-(u-p_1)^2} + p_3 e^{-(u-p_2)^2}$	3

the probability density parametrised by the set of parameters $\{p_i\}_{i=1 \dots N}$. Of course, the fitting is meaningful only as long as the number of observed quantities M is sufficiently greater than the number of fitted parameters N . For example, an exponential PDF reads

$$f_e(u, p_1) = C(p_1) \exp(-p_1 u) \quad (15)$$

with the normalisation constant

$$C(p_1) = 1 / \sum_{u \geq 3}^{u \leq 40} \exp(-p_1 u). \quad (16)$$

We then computed observable quantities averaged over the PDF of shocks as

$$\bar{X}_j(\{p_i\}_{i=1 \dots N}) = \sum_{u \geq 3}^{u \leq 40} X(u) f(u, \{p_i\}_{i=1, N}). \quad (17)$$

To facilitate the fitting process, we normalised the above values to the sum of the observable quantities:

$$\hat{X}_j = \frac{\sum_{j=1 \dots M} X_j^0}{\sum_{j=1 \dots M} \bar{X}_j}, \quad (18)$$

where $\{X_j^0\}_{j=1 \dots M}$ are the actual observed values. Note that this normalisation renders the normalisation constant of each PDF irrelevant, but it decreases the number of degrees of freedom by one unit $M_{\text{free}} = M - N - 1$. We finally find the optimal set of parameters $\{p_i^0\}_{i=1 \dots N}$ which minimises the quantity

$$\chi^2(\{p_i\}_{i=1 \dots N}) = \frac{1}{M_{\text{free}}} \sum_{j=1 \dots M} (\log_{10} \hat{X}_j - \log_{10} X_j^0)^2 / W_j^2,$$

where W_j is the uncertainty on the observed value $\log_{10} X_j^0$. We also retrieved estimates $\{E_i\}_{i=1 \dots N}$ of the errors on the parameters by computing the diagonal elements of the covariance matrix of $\frac{\partial^2 \chi^2}{\partial p_i^2}$ on the optimal set.

Table 4 summarises the various PDFs and their parametrisation. The exponential and power-law PDFs are motivated by the above mentioned work on the statistical distribution of shocks in numerical and laboratory experiments. The piece-wise exponential PDF is built in intervals designed such that the observable quantities vary significantly (cf. Figs. 3 and 7). Otherwise, the parameters would be degenerate. We used as parameters the PDF value at the transition between these intervals. Thus, these parameters' optimal values and corresponding error bars directly probe the PDF and its uncertainty at these chosen locations. Finally, we used a single or a double Gaussian PDF to mimic the fit of one shock or two independent shocks: this allows one to connect with the work of Guillard et al. (2009).

In addition, we note that the choice of the boundaries (upper and lower velocities) for the range of our grid of models does not significantly affect our results. This is because the shock emission is very low at low velocity and high-velocity shocks are very rare in the solutions we obtain. Finally, grids of models with velocity spacings of 1 km s^{-1} and 0.5 km s^{-1} gave similar results, which validates the resolution we chose.

4.2. Applications

4.2.1. Stephan's Quintet galaxy collision

In this section we use our model results to fit H_2 line emission from the galaxy-wide shock in SQ. This shock structure, first identified in radio continuum observations and X-ray images, was discovered to be a luminous H_2 source with *Spitzer* (Appleton et al. 2006; Cluver et al. 2010). It is associated with the entry of a galaxy into a group of interacting galaxies with a relative velocity $\sim 1000 \text{ km s}^{-1}$. The luminosity of the molecular gas in H_2 rotational lines is observed to be higher than that of the plasma in X-rays. Guillard et al. (2009) presented a first interpretation where the H_2 emission is powered by dissipation of turbulence driven by the large-scale collision. CO observations have since shown that the kinetic energy of the molecular gas is larger than the thermal energy of the hot (X-ray emitting) plasma. It is the main energy reservoir available to power the H_2 line emission (Guillard et al. 2012). Guillard et al. (2009) showed that the H_2 excitation is well fitted by a combination of two MHD shocks with velocities of 5 and 20 km s^{-1} in dense gas ($n_{\text{H}} \sim 10^3$ to 10^4 cm^{-3}), using the shock models of Flower & Pineau des Forêts (2003), which do not take into account UV radiation. Our grid of models allows us to test an alternative interpretation where the H_2 emission is accounted for with MHD shocks in lower density UV irradiated gas. In doing so, we quantify a solution where the physical state of the H_2 gas in SQ is akin to that of the cold neutral medium in the Galaxy. Evidence that the gas is magnetised comes from radio continuum observations. The synchrotron brightness of the shock yields a magnetic field value $B \sim 10 \mu\text{G}$, assuming equipartition of magnetic and cosmic-ray energy (Xu et al. 2003). This value is comparable to the field strength reported by Crutcher et al. (2010) for the Galactic diffuse ISM. The mean UV radiation field in the SQ shock estimated to be $G_0 = 1.4$ (Guillard et al. 2010), is also close to the reference value for the ISM in the solar neighbourhood.

The wide extension (30 kpc) of the SQ shock suggests that in the relaxation layer that follows the main high-velocity ($\sim 600 \text{ km s}^{-1}$) shock, a large number of substructures are formed that then collide and yield a range of subshocks with much lower velocities (see Guillard et al. 2009). Simulations of large-scale shocks subject to thermal instability indeed show that turbulence is sustained in the trailing relaxation layer (Koyama & Inutsuka 2002; and later Audit & Hennebelle 2005, 2010; Hennebelle & Audit 2007). This connects with the theoretical work on turbulence mentioned above, and justifies our investigation with continuous PDFs of shock velocities. The observable targets that we aim to reproduce are the emission values for the six H_2 lines 0-0 $S(0)$ to $S(5)$ in Table 1 of Cluver et al. (2010), which are integrated over the main shock structure.

Table 5 shows the best χ^2 obtained in all our attempts to fit the data. Two solutions stand out with χ^2 values reasonably close to one, the piece-wise exponential and the two Gaussians at $b = 1$ and $n_{\text{H}} = 10^2 \text{ cm}^{-3}$ (their χ^2 values are emphasised in bold faces in Table 5). Figure 9 illustrates the quality of the fit

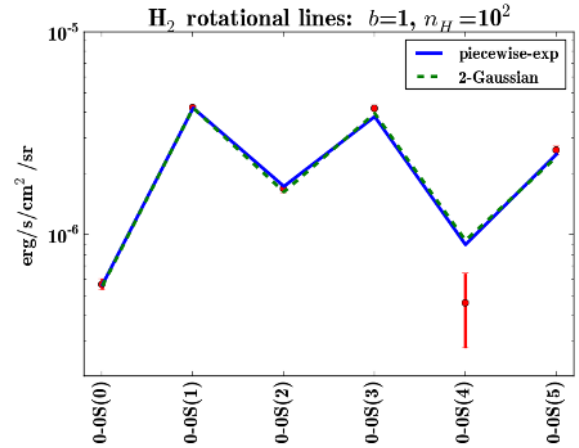


Fig. 9. Observed fluxes of the H_2 lines in the SQ (red dots with error bars: Cluver et al. 2010, see also Table 6) with the results of our best two models. Most error bars are so small they are barely visible.

on the observed H_2 -lines. Our models reproduce every H_2 -line quite accurately except for 0-0 $S(4)$ ². For comparison, when we use the same technique and same grid of models as Guillard et al. (2009) (i.e.: models without irradiation at $n_{\text{H}} = 10^4 \text{ cm}^{-3}$), we find that the best fit is obtained for two shocks of velocity 5 and 22 km s^{-1} in proportion 1:0.008 with a reduced $\chi^2 = 78$ (compared to $\chi^2 = 15.8$ for velocities 3.7 and 21 km s^{-1} in proportion 1:0.0002 in our two-Gaussians high-density case). The coincidence of the best parameters with our two-Gaussian solution is surprising, but the improvement on the χ^2 in the present work is also striking. Irradiation does indeed improve the comparison with the observations. Our work also shows that low-density solutions are even more viable than the previously found high-density solutions.

All best PDF shapes we found (including those with a high χ^2) are statistically biased towards low-velocity shocks. Figure 10 displays the two best-fit PDF solutions. The error bars (grey regions in these figures) are determined as follows: we varied the parameters of the PDFs at the extreme of their $3\text{-}\sigma$ range of uncertainty and assumed the lowest and highest values predicted when using these extreme PDFs. The piece-wise exponential adjustment shows a dip at 10 km s^{-1} , which indicates a bimodal distribution of shocks consistent with the two-Gaussian fit (which is bimodal in essence). Perturbation tests of this fit show that the PDF level at 10 km s^{-1} depends mainly on the ratio $S(0)/S(1)$, with a deeper dip for higher values of this ratio. On the other hand, the currently observed data do not distinguish whether the distribution of moderate velocity shocks is widespread or clearly centred on a distinct velocity. Indeed, as seen in Fig. 7b, above 20 km s^{-1} the emission properties of the observed H_2 lines do not change with velocity, hence these lines cannot probe the shape of the PDF in this range of velocities. Ro-vibrational lines should be used to probe the shocks at these velocities. All piecewise-exponential solutions (including those with a higher χ^2 at higher densities) are similarly consistent with bimodal distributions. This is not expected from the statistics of shock velocities in numerical simulations of turbulence. It may be a result of the intrinsic multiphase nature of the interstellar medium, where the moderate velocity shocks would be interpreted as collisions between molecular clouds, and low-velocity

² This line lies at the position of the $7.7 \mu\text{m}$ PAH emission feature, which makes it difficult to measure accurately.

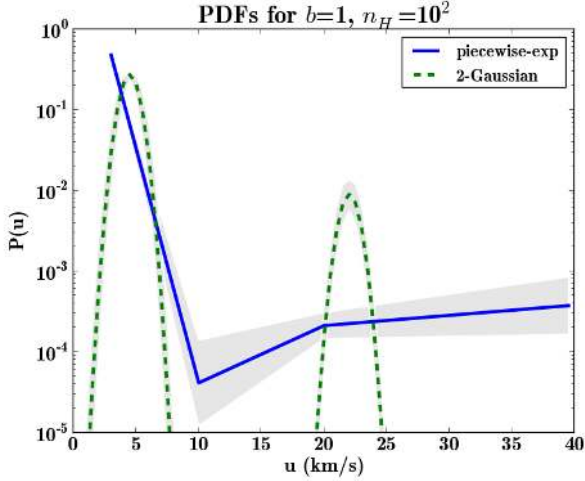


Fig. 10. Shape of our best two PDFs fit to the SQ data. Grey areas represent uncertainties due to the propagation of observational errors (see details in text).

shocks would be the signature of turbulence dissipation within these clouds.

For each of the best PDF found, we can predict the value \hat{X} of other quantities of interest. We provide in Table 6 the total column densities for some molecules and the expected emission of some atomic lines in our best two solutions. These total column densities are integrated from the pre-shock to the point where the temperature decreases to 20% above the pre-shock temperature. In particular, we provide a measure of the total H_2 column density: the piece-wise exponential model yields

$$N_{\text{shocked}}(H_2) = 2.6 \times 10^{20} \text{ cm}^{-2}$$

and the two-Gaussian model yields

$$N_{\text{shocked}}(H_2) = 1.0 \times 10^{20} \text{ cm}^{-2}.$$

Recent measurements from CO spectroscopy (Guillard et al. 2012) allow one to estimate the total H_2 column density in the SQ large-scale shock structure as

$$N_{\text{total}}(H_2) = 8.5 \times 10^{20} \pm 1.5 \times 10^{20} \text{ cm}^{-2}$$

(assuming a Galactic value for the CO emission to H_2 column conversion factor). This puts the fraction of shocked gas in this line of sight between 32% and 12%, depending on which model we adopt, which confirms the results of Guillard et al. (2010) that quite substantial amounts of gas are shock-heated. Indeed, quite a few of our best solutions predict $N_{\text{shocked}}(H_2) > 10^{21} \text{ cm}^{-2}$ and are therefore probably ruled out (only the viable solutions are underlined in Table 5).

Since the shocks account for a significant fraction of the gas mass, any chemical enhancement in the shocks may have a significant contribution to molecular abundances. Table 6 also gives estimates of the chemical yields in these shocks. For example, the H_2O abundance is about 10^{-6} , significantly greater than that observed in the diffuse ISM in the Milky-Way (Wyrowski et al. 2010). These abundances could be even higher if the medium is clumped (and therefore shielded), and *Herschel* may provide a good opportunity to test this. For standard irradiation C^+ is the dominant carbon gas species, which is also a result that will depend on shielding.

The importance of these species (in addition to H_2) as cooling agents of the interstellar turbulence directly depends on their abundance. *Herschel* observations could thus provide additional

Table 5. Summary of the best χ^2 values obtained in all our attempts to fit the SQ data.

b	n_H	one-Gauss	pow-law	exp.	pw-exp.	two-Gauss
0.1	10^2	<u>371.8</u>	2307.0	54.3	60.8	11.2
0.1	10^3	<u>504.0</u>	1650.4	152.4	61.1	105.6
0.1	10^4	<u>416.1</u>	<u>2139.9</u>	174.3	580.8	155.3
1	10^2	1628.5	<u>184.2</u>	598.5	2.6	2.0
1	10^3	139.3	175.1	35.9	<u>5.0</u>	<u>13.8</u>
1	10^4	130.3	1648.0	12.6	6.3	<u>15.8</u>

Notes. Our two best values are emphasised in bold face. n_H is given in cm^{-3} . Underlined values correspond to solutions with $N(H_2) \leq 10^{21} \text{ cm}^{-2}$.

Table 6. Results of our best two fits to the observed spectral line energy distribution in SQ and their respective predictions.

Name	pw-exp	2-Gauss	obs.	err.
H ₂ -lines observations (erg cm ⁻² s ⁻¹ sr ⁻¹)				
0-0S(0)	5.7(-7)	5.6(-7)	5.8(-7)	3.5(-8)
0-0S(1)	4.2(-6)	4.2(-6)	4.3(-6)	4.8(-8)
0-0S(2)	1.7(-6)	1.7(-6)	1.7(-6)	7.0(-8)
0-0S(3)	3.8(-6)	4.0(-6)	4.2(-6)	1.5(-7)
0-0S(4)	9.0(-7)	9.4(-7)	4.7(-7)	1.8(-7)
0-0S(5)	2.5(-6)	2.4(-6)	2.6(-6)	1.3(-7)
Predictions				
Column densities (cm ⁻²)				
H ₂ (0, 0)	5.8(19)	2.2(19)	–	–
H ₂ (0, 1)	1.8(20)	7.6(19)	–	–
H ₂ (0, 2)	3.4(18)	3.4(18)	–	–
$N(H_2)$	2.5(20)	1.0(20)	<1.0(21)	–
$N(H)$	4.3(19)	1.8(19)	–	–
$N(C^+)$	7.6(16)	3.2(16)	–	–
$N(CO)$	2.5(14)	1.8(14)	–	–
$N(H_2O)$	1.6(14)	1.9(14)	–	–
$N(OH)$	1.9(14)	1.7(14)	–	–
$N(CH)$	2.1(13)	1.0(13)	–	–
$N(CH^+)$	1.7(12)	1.1(12)	–	–
$N(HCO^+)$	7.4(11)	6.2(11)	–	–
Atomic lines (erg cm ⁻² s ⁻¹ sr ⁻¹)				
S(25.2 m)	1.4(-8)	7.0(-9)	–	–
Si+(34.8 m)	9.8(-8)	7.9(-8)	1.6(-6)	5(-8)
O(63.2 m)	1.4(-6)	9.5(-7)	–	–
O(145.3 m)	1.2(-7)	9.0(-8)	–	–
C+(158 m)	3.4(-6)	2.2(-6)	–	–
C(370.4 m)	4.6(-8)	3.1(-8)	–	–
C(609.8 m)	2.2(-8)	1.3(-8)	–	–
Integrated molecular cooling (erg cm ⁻² s ⁻¹ sr ⁻¹)				
E(H ₂)	1.6(-4)	5.4(-5)	–	–
E(CO)	4.4(-8)	2.9(-8)	–	–
E(H ₂ O)	1.1(-7)	1.0(-7)	–	–
E(OH)	4.1(-7)	1.0(-7)	–	–

Notes. Fluxes are given in $\text{erg cm}^{-2} \text{ s}^{-1} \text{ sr}^{-1}$, column densities are in cm^{-2} and cooling is indicated in $\text{erg cm}^{-2} \text{ s}^{-1} \text{ sr}^{-1}$. Parentheses denote powers of ten.

constraints to achieve a precise modelling of the physical and chemical state of the gas. We provide estimates of the total integrated flux in the molecular cooling agents in Table 6: H_2 itself is responsible for more than 94% of the cooling in both our best-fit models. However, its emission is distributed over many different lines, the strongest of which, H_2 -S(1), contributes by a few percent of the total. For low-velocity C-type shocks

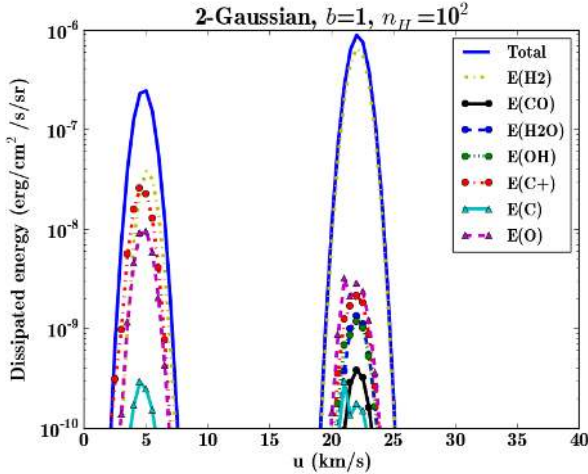


Fig. 11. Distribution of the energy dissipated via several cooling agents for the two-Gaussian best-fit model.

the pure rotational lines add up to almost the entire H_2 cooling. In contrast, moderate velocity J-type shocks experience much higher temperatures, and the energy in these shocks is radiated away through higher H_2 -levels. If our models with a contribution from moderate velocity J shocks hold, much more energy should be emitted from higher excitation levels of the H_2 molecule than is observed from pure rotational lines. Finally, other molecular coolants contribute at most a few percent of the H_2 -S(1) luminosity.

The emission of the C^+ line at $158 \mu\text{m}$ is quite strong in our best two models (about half as strong as the H_2 -S(1) line), and so is the OI emission to a lesser extent. Assuming all carbon is in the form of C^+ in the unshocked fraction of the total line of sight column density $N_{\text{total}}(\text{H}_2)$, we predict that the C^+ line should shine about as much as the H_2 -S(1) line, with a significant contribution from shocks (66% and 52% in the two models). Interestingly, this was also suggested in an interpretation of AKARI observations by Suzuki et al. (2011). In contrast, the model proposed by Guillard et al. (2009) without UV irradiation has no CII emission. This means that C^+ can indeed be a good signature for the dissipation of kinetic and magnetic energy in weakly shielded gas (as previously found by Falgarone et al. 2007). We also note that our viable models at higher densities predict even stronger emission in C^+ by up to a factor of three. As such, C^+ emission measurements will help to probe both the density and shielding of the gas. In contrast to C^+ , the measured emission of the Si^+ line at $34.8 \mu\text{m}$ is much higher than the predicted emission from our shock models. It is probably dominated by the contribution from the hot ionised medium, as already suggested by Cluver et al. (2010).

Figure 11 displays the distribution of energy radiated away for several cooling agents in the best-fit two-Gaussian solution. A significant fraction of energy is dissipated in low-velocity shocks, but more energy is radiated within moderate velocity shocks. Indeed, the dissipated power behaves as the cube of the velocity, which slightly more than compensates for the higher number of low-velocity shocks. The figure clearly demonstrates that H_2 is by far the main cooling agent. It also shows that the emission from atomic cooling agents comes mainly from low-velocity shocks, whereas the molecular emission is dominated by moderate velocity shocks. Similarly, we have checked that the emission from low J H_2 -lines probe low-velocity shocks, whereas higher J lines probe higher velocity shocks, which seems rather natural.

4.2.2. Chamaeleon

Nehmé et al. (2008) successfully interpreted observational results of a line of sight sampling diffuse molecular gas in front of the star HD 102065 in Chamaeleon. Their PDR model with $G_0 = 0.4$, $n_{\text{H}} = 80 \text{ cm}^{-3}$ and $A_v = 0.67$ accurately reproduced as many as seven independent observational quantities. However, the authors were unable to account for the column densities of rotationally excited states of H_2 and failed to reproduce the observed abundance of CH^+ . Here, we assumed that both a PDR and a statistical distribution of shocks contribute to this line of sight. Hence we attempted to fit as many as 11 observational measurements available for this line of sight with a linear combination of our shock models and a PDR model.

The PDR model was computed with our shock code in a PDR mode, see Sect. 2.1. In principle, we should fit all irradiation parameters of the PDR alongside the grid of shocks. But this would entail recomputing the whole grid of shocks each time we probe new irradiation parameters and would lead to prohibitive computational times. Hence we fixed the irradiation conditions and the PDR model therefore introduces only one additional parameter in the fit: its weight in the line of sight compared to the shock models. We used $G_0 = 4$ and $A_v = 0.335$ as entrance conditions for both the PDR and the shocks and computed a new grid of shock models from 3 to 40 km s^{-1} with $n_{\text{H}} = 80 \text{ cm}^{-3}$ and an ortho/para ratio of 0.7 as observed.

We thus obtained reasonable χ^2 values with a best value of 11 for both the two-Gaussian and the piecewise-exponential. The error mainly comes from overestimating the column density in $J = 5$, but the molecular chemistry of the line of sight is reproduced quite accurately (see Table 7).

The two best-fitting PDFs compare qualitatively well to the solutions we found for SQ, except that the low-velocity part of the two-Gaussian is more tightly peaked on low velocities (the moderate-velocity component accounts for 3% of the total probability), and the piecewise-exponential dip at 10 km s^{-1} is less pronounced. The two PDF shapes are hence slightly less consistent than for SQ, and continuous solutions are not ruled out (the exponential and power-law solutions yield χ^2 values of about 20 and 15). However, for the Chamaeleon, the physical extent of the measured beam is much smaller than for SQ. In particular, the total number of shocks involved is presumably much smaller and discrete number effects might appear in the distribution.

Our best two models predict similar values for most of the observables listed in Table 7. We now have two contributions from the PDR and the shocks, and for each quantity listed in Table 7 we quote in brackets which fraction comes from the shocks. The weight of the PDR model in both best solutions is slightly different, which yields a mass fraction of shocked matter on the line of sight of 4% in the piecewise-exponential model and 19% in the two-Gaussian model. The contribution from shocks is hence small but not insignificant. However, molecules other than H_2 are all formed in the shocks and not in the PDR, with 98% of the CO coming from the shocks, for example. In our two best models, shocks with velocity above 15 km s^{-1} account for the formation of almost all molecules. This is because the chemical barriers are overcome thanks to the thermal energy released in shocks and thanks to the ions-neutrals drift, as mentioned in Sects. 3.4 and 3.5.

CH^+ needs a mechanical energy injection to raise the effective temperature for its formation, which is why pure PDR models failed to account for its abundance. Indeed, CH^+ forces a component into the model that is too hot, which then overproduces the $J = 5$ H_2 -level. A possible solution would be that the

Table 7. Results and predictions of the fit of piecewise-exponential to the Chamaeleon data (Gry et al. 2002; Nehmé et al. 2008).

Names	Piecewise-exp	Two-Gaussian	Obs	Error
Column densities (cm ⁻²)				
Observations				
<i>N</i> (H)	2.6(20) [0.06]	2.7(20) [0.23]	3.1(20)	3.0(19)
H ₂ (0,0)	1.8(20) [0.04]	1.8(20) [0.20]	2.0(20)	2.0(19)
H ₂ (0,1)	2.1(20) [0.03]	1.9(20) [0.14]	1.4(20)	1.0(19)
H ₂ (0,2)	2.6(18) [0.53]	2.6(18) [0.61]	2.6(18)	1.0(17)
H ₂ (0,3)	4.2(17) [0.99]	4.9(17) [0.99]	2.0(17)	1.0(17)
H ₂ (0,4)	4.4(16) [1.00]	5.9(16) [1.00]	2.0(16)	1.0(16)
H ₂ (0,5)	2.2(16) [1.00]	3.8(16) [1.00]	7.1(14)	5.0(14)
<i>N</i> (C)	2.4(15) [0.20]	2.3(15) [0.30]	6.0(14)	1.5(14)
<i>N</i> (CO)	5.2(13) [0.98]	4.9(13) [0.98]	5.6(13)	6.8(12)
<i>N</i> (CH)	6.2(12) [0.87]	4.8(12) [0.86]	6.4(12)	1.0(12)
<i>N</i> (CH+)	8.8(12) [1.00]	1.0(13) [1.00]	1.2(13)	1.9(12)
Predictions				
<i>N</i> (H ₂)	3.9(20) [0.04]	3.8(20) [0.17]	–	–
<i>N</i> (C+)	1.4(17) [0.05]	1.4(17) [0.19]	–	–
<i>N</i> (H ₂ O)	2.8(13) [0.99]	5.3(13) [1.00]	–	–
<i>N</i> (OH)	6.9(13) [0.99]	1.1(14) [0.99]	–	–
<i>N</i> (HCO+)	2.7(11) [0.99]	3.4(11) [0.99]	–	–
<i>N</i> (CN)	3.9(11) [0.99]	5.3(11) [0.99]	<5.9(11)	–
<i>N</i> (C ₂)	3.6(10) [0.80]	2.8(10) [0.77]	<1.4(13)	–
Atomic lines (erg cm ⁻² s ⁻¹ sr ⁻²)				
S(25.2 m)	4.5(–9) [1.00]	5.1(–9) [1.00]	–	–
Si+(34.8 m)	6.4(–8) [0.82]	6.0(–8) [0.84]	–	–
O(63.2 m)	1.2(–6) [0.66]	1.1(–6) [0.67]	–	–
O(145.3 m)	8.7(–8) [0.76]	7.7(–8) [0.77]	–	–
C+(158 m)	3.8(–6) [0.18]	3.9(–6) [0.31]	2.8(–6)	–
C(370.4 m)	2.2(–8) [0.60]	2.3(–8) [0.68]	–	–
C(609.8 m)	1.3(–8) [0.33]	1.3(–8) [0.44]	–	–
Molecular cooling (erg cm ⁻² s ⁻¹ sr ⁻¹)				
0-0S(1)	1.9(–6) [0.99]	2.2(–6) [0.99]	–	–
E(H ₂)	9.5(–5) [1.00]	5.7(–5) [0.99]	–	–
E(CO)	9.3(–8) [1.00]	8.5(–8) [1.00]	–	–
E(H ₂ O)	1.8(–7) [1.00]	2.3(–7) [1.00]	–	–
E(OH)	2.9(–6) [1.00]	2.0(–6) [1.00]	–	–

Notes. Powers of ten are indicated in parentheses. For each value, we provide the fraction coming from the shocks in brackets.

irradiation in the far-UV is enhanced in the Chamaeleon compared to the Draine ISRF: this would make more CH⁺ from CH₂⁺ and CH₃⁺ photo-dissociation (Falgaroni et al. 2010) while requiring a lower temperature more compatible with the observed $J = 5$ H₂-level column density. Indeed, UV spectra in Boulanger et al. (1994) suggested that the enhanced far-UV field could be accounted for by a flatter extinction curve in the far-UV for this very line of sight.

As in SQ, H₂ is by far the main cooling agent (it radiates more than 92% of the total cooling in the two best-fit models), but CII (and OI to a lesser extent) has an emission comparable to the H₂-S(1) line. Even though it is dominated by the emission from the PDR, the shock contribution to CII emission is still significant (from 18% to 31% according to the two best models). Interestingly, we predict that OH will shine about as much as CII, and as for the SQ solution, the OH emission is almost completely dominated by the contribution from shocks at moderate velocity. OH observations would hence provide a good test of the possible existence of a moderate-velocity shock component in the Chamaeleon.

5. Summary, conclusions, discussion, and prospects

We provide a grid of shock models³ in UV-heated gas that may be used to interpret observations of the Milky Way diffuse ISM and integrated properties of galaxies in general. We examined magnetised shocks in media with densities from $n_{\text{H}} = 10^2$ to 10^4 cm⁻³, with standard ISM irradiation conditions and at low- to moderate velocities (from 3 to 40 km s⁻¹). When the velocity of these shocks was below the critical velocity for the existence of pure C-type shocks, we computed C-type shocks, otherwise, we computed J-type shocks. The models include the effects of the ambient UV irradiation field on the pre-shock chemistry and thereby on the relative importance of cooling lines in the shock. For instance, C⁺ can provide significant line cooling in shocks propagating in the UV-irradiated gas, where it is the dominant carbon species.

We illustrated how the model results may be used to interpret data on one galactic line of sight through the diffuse ISM (Chamaeleon) and one extra-galactic object (the SQ shock). We fitted the observables with a continuous combination of shock models as a phenomenological description of the complex statistical properties of the turbulence dissipation. The model provides quite a good match to the data for bimodal distributions of shock velocities. This does not agree with predictions from numerical simulations of Smith et al. (2000), who found a power-law distribution with an exponential cut-off. More work is needed to understand the reasons behind this apparent discrepancy. Interestingly, the low- and moderate velocity components of our best-fit PDF operate in very different regimes of energy dissipation. Indeed, in our best-fit models to the observations, the low-velocity shocks are of C-type and dissipate energy via ion-neutral drift, whereas the higher velocity shocks are of J-type and undergo viscous dissipation.

In both our interpretations of SQ and the Chamaeleon, a significant fraction of the molecular gas is shock-heated, and the chemistry in this shock-heated gas has a dominant contribution to key molecules such as CO, H₂O, OH or CH⁺, which are commonly used as diagnostics. This shock-heated contribution might be greater than the contribution of CO computed in simulations by Glover & Mac Low (2011), where the resolution in the shocks is too low to trigger the shock chemistry: an insufficiently low resolution smears out the temperature to such an extent that shocks become nearly isothermal with a temperature too low for molecule formation. Furthermore, although low-velocity shocks are less efficient than moderate-velocity shocks, they are more numerous, and depending on the statistical distribution of shocks they could potentially account for a higher fraction of the excitation and formation of molecules.

Shocks in the line of sight also have important consequences on the emission of C⁺. Indeed, C⁺ is usually considered as a good tracer of the ambient UV radiation field, and indeed, the mere presence of the C⁺ ion is conditioned to its photo-ionisation. But we showed here that the emission of C⁺ in both SQ and Chamaeleon has a significant contribution from gas heated by the dissipation of kinetic energy rather than by UV photons, as is the case in PDRs.

The SQ H₂ excitation diagram was fitted with low- and moderate-velocity C shocks in dense UV-shielded gas ($n_{\text{H}} = 10^4$ cm⁻³, $G_0 = 0$) in previous studies (Guillard et al. 2009). We showed that a better fit can be obtained with diffuse irradiated

³ The output data at our models are archived on <http://cemag.ens.fr> and at the CDS.

gas ($n_{\text{H}} = 10^2 \text{ cm}^{-3}$, $G_0 = 1$) including J-type shocks. If this second solution is the appropriate one, C^+ is a significant coolant of the shocked medium. This prediction can be tested with the *Herschel* observatory. The presence of the high-velocity J shocks can also be tested through the emission in H_2 -lines coming from rovibrational levels.

OI, H_2O , OH, and CO provide additional diagnostic lines that could help in constraining the physical state of the gas and the dissipation processes. OI is seen to be significant at higher densities, whereas C^+ is significant for lower densities. Molecules such as H_2O , OH, and CO evacuate less than one percent of the total kinetic power except at high densities where H_2O in C shocks can contribute as much as 10%.

The remainder of the incoming power in our shocks is converted into a flux of magnetic energy. The differences in total pressure (magnetic plus thermal) between the shocked regions and the regions that have not been shocked will initiate new motions: the energy stored in the post-shock compression will eventually give rise to expansion motions, with an effective transfer back to kinetic energy. Thus, shocks are actors that contribute to the equipartition between various forms of energy, thanks to a continuous recycling of the gas throughout successive shock structures.

The main caveat of our study is that we assumed the relaxation of the post-shock pressure takes place instantaneously: our model accounts for the pre-shock gas and the shocked gas, but does not incorporate the expansion of the gas after the shock. We will attempt to model this phase in future studies. Another caveat of our study lies in the implicit assumption that all shocks are steady. Indeed, some shock velocities are prone to instabilities and even quasi-steady models are invalid in this case (see [Lesaffre et al. 2004b](#), for example). Less important caveats are the shock orientation, its curvature, the neglect of intermediate ages of shocks (for ages younger than about 10^4 yr, we should consider CJ-type shocks or non-steady shocks). We believe that these minor caveats are balanced because we fitted a statistical collection of shock velocities. Finally we did not treat UV pumping in the H_2 -population, but [Monteiro et al. \(1988\)](#) showed that this begins to make a difference only for H_2 levels above $J = 5$ and for $G_0 \gg 1$.

Our PDF fitting technique might prove useful to account for single shocks with more complicated geometries. For example, a single bow-shock effectively encompasses a continuous collection of velocities depending on the angle at which each fluid parcel of pre-shock gas impinges on the bow-shock. In this framework, the shape of the lines is directly related to the dynamics inside the shock, and not simply due to the relative motions between each shocks as in the statistical distribution of shocks we inferred in SQ. In these cases, it will therefore be interesting to predict and use the line shapes as additional observational constraints on the shock physics.

Finally, as we already mentioned, the dissipation of turbulent motions does not occur in shocks only. It will be interesting in future work to assess on the one hand the fraction of the energy dissipation that takes place in vortices, current sheets, or shocks, for example. On the other hand, it will be worth comparing vortex models as in [Godard et al. \(2009\)](#) to our own shock models to check whether we can observationally distinguish the respective signatures of shocks and vortices.

Acknowledgements. P.L., E.F., and B.G. acknowledge support from SCHISM A.N.R.. We thank Maryonne Gerin and Antoine Gusdorf for comments on the manuscript. We thank the anonymous referee for his/her comments, which improved the readability of the paper.

References

- Abrahamsson, E., Krems, R. V., & Dalgarno, A. 2007, *ApJ*, 654, 1171
 Agúndez, M., Goicoechea, J. R., Cernicharo, J., Faure, A., & Roueff, E. 2010, *ApJ*, 713, 662
 Appleton, P. N., Xu, K. C., Reach, W., et al. 2006, *ApJ*, 639, L51
 Audit, E., & Hennebelle, P. 2005, *A&A*, 433, 1
 Audit, E., & Hennebelle, P. 2010, *A&A*, 511, A76
 Bergin, E. A., Hartmann, L. W., Raymond, J. C., & Ballesteros-Paredes, J. 2004, *ApJ*, 612, 921
 Black, J. H., & van Dishoeck, E. F. 1987, *ApJ*, 322, 412
 Boulanger, F., Prevot, M. L., & Gry, C. 1994, *A&A*, 284, 956
 Chièze, J.-P., Pineau des Forêts, G., & Flower, D. R. 1998, *MNRAS*, 295, 672
 Cluver, M. E., Appleton, P. N., Boulanger, F., et al. 2010, *ApJ*, 710, 248
 Crutcher, R. M., Wandelt, B., Heiles, C., Falgarone, E., & Troland, T. H. 2010, *ApJ*, 725, 466
 Draine, B. T. 1978, *ApJS*, 36, 595
 Draine, B. T. 1980, *ApJ*, 241, 1021
 Draine, B. T., & Bertoldi, F. 1996, *ApJ*, 468, 269
 Draine, B. T., Roberge, W. G., & Dalgarno, A. 1983, *ApJ*, 264, 485
 Falgarone, E., Verstraete, L., Pineau des Forêts, G., & Hily-Blant, P. 2005, *A&A*, 433, 997
 Falgarone, E., Hily-Blant, P., Pety, J., & Pineau des Forêts, G. 2007, in *IAU Symp. 237*, eds. B. G. Elmegreen, & J. Palous, 24
 Falgarone, E., Ossenkopf, V., Gerin, M., et al. 2010, *A&A*, 518, L118
 Flower, D. R., & Pineau des Forêts, G. 2003, *MNRAS*, 343, 390
 Flower, D. R., & Pineau des Forêts, G. 2010, *MNRAS*, 406, 1745
 Flower, D. R., Pineau des Forêts, G., & Hartquist, T. W. 1985, *MNRAS*, 216, 775
 Flower, D. R., Pineau-des-Forêts, G., & Hartquist, T. W. 1986, *MNRAS*, 218, 729
 Flower, D. R., Le Bourlot, J., Pineau des Forêts, G., & Cabrit, S. 2003, *MNRAS*, 341, 70
 Gerlich, D., Disch, R., & Scherbarth, S. 1987, *J. Chem. Phys.*, 87, 350
 Glover, S. C. O., & Mac Low, M.-M. 2011, *MNRAS*, 412, 337
 Godard, B., Falgarone, E., & Pineau des Forêts, G. 2009, *A&A*, 495, 847
 Godard, B., Falgarone, E., Gerin, M., et al. 2012, *A&A*, 540, A87
 Gredel, R., Pineau des Forêts, G., & Federman, S. R. 2002, *A&A*, 389, 993
 Gry, C., Boulanger, F., Nehmé, C., et al. 2002, *A&A*, 391, 675
 Guillet, V., Pineau des Forêts, G., & Jones, A. P. 2007, *A&A*, 476, 263
 Guillard, P., Boulanger, F., Pineau des Forêts, G., & Appleton, P. N. 2009, *A&A*, 502, 515
 Guillard, P., Boulanger, F., Cluver, M. E., et al. 2010, *A&A*, 518, A59
 Guillard, P., Boulanger, F., Pineau des Forêts, G., et al. 2012, *ApJ*, 749, 158
 Heck, L., Flower, D. R., & Pineau des Forêts, G. 1990, *Comput. Phys. Commun.*, 58, 169
 Hennebelle, P., & Audit, E. 2007, *A&A*, 465, 431
 Hierl, P. M., Morris, R. A., & Viggiano, A. A. 1997, *J. Chem. Phys.*, 106, 10145
 Hollenbach, D., & McKee, C. F. 1989, *ApJ*, 342, 306
 Ingalls, J. G., Bania, T. M., Boulanger, F., et al. 2011, *ApJ*, 743, 174
 Jenkins, E. B. 2009, *ApJ*, 700, 1299
 Koyama, H., & Inutsuka, S.-i. 2002, *ApJ*, 564, L97
 Le Petit, F., Nehmé, C., Le Bourlot, J., & Roueff, E. 2006, *ApJS*, 164, 506
 Lee, H.-H., Herbst, E., Pineau des Forêts, G., Roueff, E., & Le Bourlot, J. 1996, *A&A*, 311, 690
 Lesaffre, P., Chièze, J.-P., Cabrit, S., & Pineau des Forêts, G. 2004a, *A&A*, 427, 147
 Lesaffre, P., Chièze, J.-P., Cabrit, S., & Pineau des Forêts, G. 2004b, *A&A*, 427, 157
 Monchick, L., & Schaefer, J. 1980, *J. Chem. Phys.*, 73, 6153
 Monteiro, T. S., Flower, D. R., Pineau des Forêts, G., & Roueff, E. 1988, *MNRAS*, 234, 863
 Mouri, H., Hori, A., & Takaoka, M. 2008, *Phys. Fluids*, 20, 035108
 Mullan, D. J. 1971, *MNRAS*, 153, 145
 Nehmé, C., Le Bourlot, J., Boulanger, F., Pineau des Forêts, G., & Gry, C. 2008, *A&A*, 483, 485
 Neufeld, D. A., & Kaufman, M. J. 1993, *ApJ*, 418, 263
 Pety, J., & Falgarone, É. 2000, *A&A*, 356, 279
 Pineau des Forêts, G., Flower, D. R., Hartquist, T. W., & Dalgarno, A. 1986, *MNRAS*, 220, 801
 Roberge, W. G., & Draine, B. T. 1990, *ApJ*, 350, 700
 Smith, M. D., Mac Low, M.-M., & Heitsch, F. 2000, *A&A*, 362, 333
 Suzuki, T., Kaneda, H., Onaka, T., & Kitayama, T. 2011, *ApJ*, 731, L12
 Wardle, M. 1998, *MNRAS*, 298, 507
 Wyrowski, F., van der Tak, F., Herpin, F., et al. 2010, *A&A*, 521, L34